Atomically Dispersed Manganese Catalysts for Oxygen Reduction in Proton Exchange Membrane Fuel Cells

Jiazhan Li[1,2,Δ], Mengjie Chen[2,Δ], David A. Cullen[3], Sooyeon Hwang[4], Maoyu Wang[5], Boyang Li[6], Kexi Liu[6], Stavros Karakalos[7], Marcos Lucero[5], Hanguang Zhang[2], Chao Lei[8], Hui Xu[8], George E. Sterbinsky[9], Zhenxing Feng[5], Dong Su[4], Karren L. More[10], Guofeng Wang[6], Zhenbo Wang[1,*] and Gang Wu[2,*]

[1] MIIT Key Laboratory of Critical Materials Technology for New Energy Conversion and Storage, School of Chemistry and Chemical Engineering, Harbin Institute of Technology, Harbin, 150001, China

[2] Department of Chemical and Biological Engineering, University at Buffalo, The State University of New York, Buffalo, NY 14260, United States

[3] Materials Science and Technology Division, Oak Ridge National Laboratory, Oak Ridge, TN 37831, United States

[4] Center for Functional Nanomaterials, Brookhaven National Laboratory, Upton, NY 11973, United States

[5] School of Chemical Biological, and Environmental Engineering, Oregon State University, Corvallis, OR 97331, United States

[6] Department of Mechanical Engineering and Materials Science, University of Pittsburgh, Pittsburgh, PA 15261, United States

[7] Department of Chemical Engineering, University of South Carolina, Columbia, SC 29208, United States
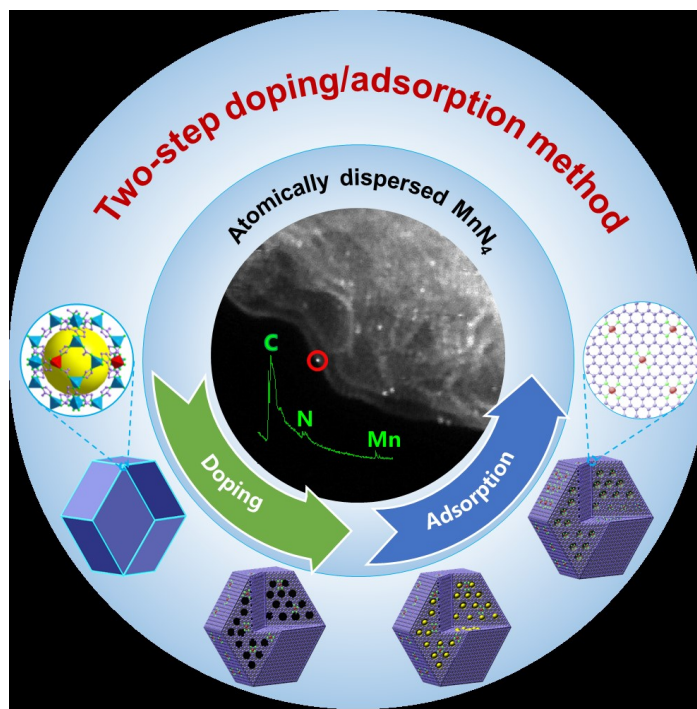
[8] Giner Inc., Newton, MA 02466, United States

[9] Advanced Photon Source, Argonne National Laboratory, Argonne IL, 60439, United States

[10.] Center for Nanophase Materials Sciences, Oak Ridge National Laboratory, Oak Ridge, TN 37831, United States

[Δ] These two authors contributed equally

Corresponding authors: wangzhb@hit.edu.cn (Z. Wang) and gangwu@buffalo.edu (G. Wu)

Graphical Abstract

Platinum group metal (PGM)-free catalysts that are also Fe-free are highly desirable for the oxygen reduction reaction (ORR) in proton exchange membrane fuel cells (PEMFCs). Because the possible Fenton reactions ($Fe^{2+}+H_2O_2$) generate free radicals, which possibly degrade the ionomer in the electrodes and the membrane in PEMFCs. In this study, inspired by theoretical predictions, a new type of atomically dispersed nitrogen-coordinated single Mn site catalyst (Mn-N-C) was derived from a metal-organic framework (MOF) through a continuous two-step doping and adsorption approach. Evidence for the embedding of the atomically dispersed MnN_4 moieties within the carbon surface-exposed basal planes was established by X-ray absorption spectroscopy and the MnN_4 dispersions were imaged by aberration-corrected electron microscopy at the atomic

level. Iterative chemical doping and subsequent adsorption are crucial for significantly increasing the density of MnN$_4$ active sites in a MOF-derived 3D porous carbon phase. The Mn-N-C catalyst thus-synthesized exhibited exceptional activity (*e.g.*, a half-wave potential, $E_{1/2}$ of 0.80 V *vs*. RHE) approaching that of Fe-N-C catalysts along with significantly enhanced stability in acidic media. The encouraging performance of the Mn-N-C catalyst as a PGM-free cathode was demonstrated in fuel cells. First principles calculations further support that these MnN$_4$ sites within optimal local carbon structures are the origin of the ORR activity in acids via a 4e$^-$ pathway. The enhanced stability is due to improved corrosion resistance of carbon in catalysts stemming from Mn doping along with intrinsic stability of MnN$_4$ sites. Therefore, the atomically dispersed Mn-N-C catalyst presents a new opportunity to developing high-performance Fe-free ORR catalysts promising to address the Fenton reagent issues and make PGM-free cathodes a viable option for PEMFCs.

Development of cost-effective and high-performance platinum group metal (PGM)-free catalysts for the sluggish oxygen reduction reaction (ORR) is key to realizing the large-scale application of proton exchange membrane fuel cells (PEMFCs).[1-6] It was reported that various defects including surface-exposed carbon basal plane edges and steps, and nitrogen doping of the carbon can facilitate the ORR by directly providing adsorption sites and/or by modifying the electronic properties of carbon.[7-10] Such metal-free active sites exhibit good ORR activity in an alkaline electrolyte, and the exposed edge carbon and those carbon atoms adjacent to nitrogen are

believed to act as preferred catalytic sites.[8,9,11] However, the activity in acidic media is not sufficient because these metal-free catalysts suffer from large overpotential mostly catalyzing the ORR *via* a two-electron pathway.[12,13] In contrast, the co-doped metal and nitrogen in carbon materials in the form of MN_xC_y can serve as point defects (substitutional impurities) and work synergistically to tune the electronic and geometric properties of carbon matrix. Importantly, the MN_xC_y moieties are believed acting as the active sites to directly adsorb O_2 and catalyze the subsequent O-O bond breaking in acid media, therefore significantly improving the ORR catalytic activity.[1,3,14-16] Synergetic effects between M and N facilitate the ORR,[16] which can be described using a Pt-N structure as a defined model. However, the bonding energies of M-N with O_2 and other ORR intermediates are largely dependent on the nature of the transition metal, which leads to significantly different activities and stabilities for $M-N_x$ sites. Among the studied transition metals, Fe or Co with N-doped carbon form the M-N-C catalysts, which are presently recognized to be the most promising PGM-free catalysts.[17,18] They exhibit encouraging ORR activities and stabilities in harsh acidic media.[19-21] Despite tremendous efforts to develop Fe-N-C and Co-N-C catalysts,[1,2,10,15,22] they still suffer from insufficient durability, especially at the desirable high voltages (>0.6 V), which limits their practical applications.[23-25] Kinetic losses primarily result from the dissolution of active metal sites[6,26] and corrosion of the carbon phases.[27] These problems may be caused by H_2O_2 oxidative attack or by protonation of the doped N neighboring the active metal sites followed by anion adsorption.[25,28] Carbon corrosion not only promotes dissolution of the active sites[29] but also induces significant charge- and mass-transport resistances due to the changes in the carbon lattice structures and morphologies .[30] Thus, a

relatively high degree of graphitization is vital for PGM-free catalyst stability to enhance the corrosion-resistance to the carbon. In addition to insufficient stability, Fe-N-C catalysts are criticized for their participation in and/or promotion of the Fenton reactions ($Fe^{2+}+H_2O_2$), where dissolved Fe ions combine with H_2O_2, a by-product of the two-electron ORR.[31] As a result, significant amount of active oxygen-containing hydroxyl and hydroperoxyl radicals are generated that can degrade the ionomer within the electrode and the polymer membrane in PEMFCs (details of the reactions and mechanisms are described in supplementary materials). Therefore, high-performance PGM- and Fe-free catalysts are highly desirable for PEMFC technologies.[32] Co-N-C catalysts are a logical alternative. However, it has been reported that Co-N-C catalysts suffer from substantial generation of H_2O_2 during the ORR in acidic media, and are thus likely to also participate in Fenton reactions.[14,33] In addition, the Co-N coordinated structures are even less stable in acids than Fe-N-C catalysts.[34] Unlike Fe and Co, Fenton reactions involving Mn ions are insignificant because of weak reactivity between Mn and H_2O_2.[33,35] Recently, we discovered that Mn doping promotes the stabilization of nanocarbon catalysts and catalyzes graphitic structures in catalysts relative to Fe and Co.[36,37] Preliminary density functional theory (DFT) calculations predicted that MnN_4 moieties embedded in carbon possess comparable activity and enhanced stability relative to FeN_4 sites. Inspired by this theoretical prediction, we hypothesized that Mn-N-C catalysts are likely more stable than Fe-N-C in harsh acidic media. However, a grand challenge is to increase the density of MnN_4 active sites because Mn atoms tend to form unstable and inactive metallic compounds, oxides and carbides during the heat treatment when simply increasing the amount of metal

precursor.[36,38,39] Thus, innovative synthesis approaches to realizing atomically dispersed single Mn sites with increased density will be crucial for high-performance Mn-N-C catalysts.

Knowledge gained through our previous studies of Fe and Co catalysts[32,40-42] have provided guidelines for the synthesis of Mn-N-C catalysts having a uniform, atomic dispersion of MnN_4 active sites within a stable graphitic carbon structural framework. For example, a zinc containing zeolitic imidazolate frameworks (ZIF-8), a type of metal-organic framework (MOF) with flexible controls of the structure and chemistry, enables the formation of atomically dispersed MN_4 active sites for Fe- or Co-N-C catalysts.[32,40,43] The unique hydrocarbon networks in ZIF precursors can be directly converted into N- and M-doped highly disordered carbon, while maintaining their original polyhedral particle shape and porous structure during the thermal activation.[44,45] Recently, innovative synthesis strategies based on ZIF-8 precursors with chemical doping and ion confinement have resulted in atomically dispersed Fe or Co sites with increased density.[2,32,40,46-50] Motivated by these successes, we explore the ZIF approach to preparing atomically dispersed Mn-N-C catalysts for the ORR in acids. However, unlike Fe and Co ions, Mn ions cannot easily exchange the original Zn and form complexes with N in the ZIF-8 precursor. Although MnN_4 sites are predicted to be active for the ORR, only a low density of atomic sites are introduced using a conventional one-step chemical doping. Due to the various Mn-valence states from 0 to +7, Mn aggregates easily form during the high temperature carbonization process, even at a relatively low Mn content. New synthetic strategies are thus required to create high-performance Mn catalysts with significantly increased active site densities. Here, we report an atomically dispersed MnN_4 catalyst with increased density through

6

an innovative two-step synthesis strategy involving doping and adsorption process that leverages the unique properties of ZIF-8 precursors. In the first step of synthesis, Mn ions are combined with Zn ions to prepare Mn-doped ZIF-8 precursors. After carbonization and acid leaching, the second step of synthesis employs the derived porous carbon as a host to adsorb additional Mn and N sources followed by a subsequent thermal activation. X-ray absorption spectroscopy (XAS) analysis indicate that the Mn species in the obtained catalysts is in the form of atomically dispersed MnN_4, which is further confirmed through medium-angle annular dark-field imaging (MAADF)-scanning transmission electron microscope (STEM) imaging coupled with electron energy loss spectroscopy (EELS). This new type of atomically dispersed Mn-N-C catalyst achieved promising activity ($E_{1/2}$=0.80 V *vs*. RHE) and excellent stability in aqueous acids as well as in an operating fuel cell. This work provides a new pathway to advance PGM- and Fe-free catalysts for future PEMFC applications.

Results

Synthesis of materials. A continuous two-step doping and adsorption approach has been developed to prepare atomically dispersed Mn-N-C catalysts as shown in **Fig. 1**. Experimental details are described in supplementary materials. In the first step, Mn-doped ZIF-8 (Mn-ZIF-8) precursors were synthesized at 120°C in a dimethylformamide (DMF) solvent consisting of zinc (II) nitrate hexahydrate and manganese (III) acetate dihydrate. Porous 3D porous nanocarbon (NC) particles were obtained by pyrolyzing the Mn-ZIF-8 precursors followed by an acid leaching treatment with samples labelled as *n*Mn-NC-first. Here, the Mn content (*n*= 0, 10, 20,

7

and 30 at.%) is controlled as a function of the total metal content (Mn and Zn) used for ZIF-8 precursor synthesis and is a critical step in this process. An optimal doping content of 20 at.% Mn yielded the best catalyst activity. In the second step of the synthesis, the Mn-NC-first samples were dispersed in a solution (isopropanol: water=1:1 in volume) containing Mn (II) chloride Mn and N sources for the adsorption followed by a thermal treatment. The final catalysts were named as nMn-NC-second. Among the studied nitrogen sources (*e.g.*, dipicolylamine, cyanamide, phenanthroline, and melamine), cyanamide yielded the highest activity of the final catalysts. The two-step synthesis procedure introduces an increased density of MnN$_x$ active sites.

Atomically dispersed and N coordinated Mn sites. Supplementary Fig. 1 presents the overall morphology of the best performing 20Mn-NC-second catalyst and shows a homogeneous distribution of polyhedral carbon particles with a size of about 50 nm, which directly transforms from the 20Mn-ZIF nanocrystal precursors with slight size reduction. The dominant diffraction peaks corresponding with carbon in the X-ray diffraction (XRD) together with the broad D and G bonds in the Raman spectra (Supplementary Fig. 2) are consistent with a partially graphitized carbon structures (meso-graphitic), which is confirmed by high-resolution scanning transmission electron microscopy (HR-STEM) images (Supplementary Fig. 1h). Both XRD and STEM verified the absence of any crystalline Mn-containing phases or clusters in the 20Mn-NC-second catalyst. In addition, the carbon particles exhibit a high degree of microporosity, an essential characteristic for increasing the amount of surface areas available for hosting active sites. The

morphology (shape and size) and structure (extent of graphitization) of carbon particles can be tuned by varying the Mn content in the first step. As shown in Supplementary Fig. 3, the carbon particle size is slightly increased by adding more Mn content. Large particles having an irregular shape appeared when the Mn content reaches 30 at.%, indicating that excess Mn ions in the solution disturb the controlled growth of the ZIF nanocrystals. Raman results further indicated that the Mn content in the first step can significantly increase the extend of graphitization in the resulting carbon structures (Supplementary Fig. 4 and Supplementary Table 1). All three of the Mn-NC-first (n= 0, 10, 20, and 30 at.%) samples exhibited much smaller ratios of G and G peak areas (Area$_D$/Area$_G$) relative to "Mn-free" 0Mn-NC. Higher Mn content doped into ZIF-8 precursors, larger degree of graphitization of the carbon particles from the pyrolysis in the first step. The carbon structures remain nearly the same after the second adsorption step of synthesis.

According to inductively coupled plasma-mass spectrometry (ICP-MS), the Mn content in the 20Mn-NC-second catalyst, which exhibited the highest catalyst activity, can be up to 3.03 wt.% (Supplementary Table 2), which is comparable to other atomically dispersed Fe and Co catalysts (Supplementary Table 3). As no significant Mn clustering was observed by HR-STEM and XRD analyses, homogeneous dispersion of atomic Mn species is likely. The oxidation state and local coordination environment of Mn in catalysts were further examined by X-ray absorption near edge structure (XANES) spectroscopy and extended X-ray absorption fine structure (EXAFS) spectroscopy using established experimental and theoretical modeling methods.[32,40,41,51,52] Several standard Mn compounds (*e.g.*, MnO, MnO$_2$, and Mn

phthalocyanine-Pc) were included in the XANES/EXAFS studies to compare with the 20Mn-NC-second catalyst. MnPc has the well-defined MnN_4 chemical structure (Supplementary Fig. 5), which provides a baseline for the bulk catalyst measurements that can be used to identify potential active sites in the 20Mn-NC-second catalyst. As shown in **Fig. 2a**, the XANFS edge profile of the 20Mn-NC-second catalyst is closer to that of Mn (II) in MnO but is far from that of Mn (IV) in MnO_2, suggesting that the oxidation state of Mn in the 20Mn-NC-second catalyst is close to 2+. **Fig. 2b** shows the EXAFS spectrum of the MnPc, which is well fitted with MnN_4 coordination (CN_{Mn-N} = 4 ± 0.4, where CN refers to coordination number and Mn-N is the scattering path). The fit is also plotted in k-space in Supplementary Fig. 5. As shown in **Fig. 2c**, the EXAFS of the 20Mn-NC-second catalyst is well represented by a combination of the Mn-N and Mn-C scattering paths (Supplementary Table 4). The first shell coordination number of Mn-N is given by CN_{Mn-N} = 3.2 ± 1.0, suggesting the dominant Mn-N structure in the 20Mn-NC-second catalyst is likely to be MnN_4. We also compared the Mn K-edge EXAFS spectra of 20Mn-NC-second to manganese nitride (Mn_4N) and metallic manganese (Mn foil) to exclude the formation of nitrides and metallic Mn (Supplementary Fig. 6). Both Mn_4N and Mn foil exhibit peaks at ~2.3 Å assigned to Mn−Mn distance, corresponding to the metallic structure. The absence of Mn-Mn peak in the 20Mn-NC-second further verifies there is no such Mn clusters in the 20Mn-NC-second catalyst. We note that the peak at around 1.9 Ångstrom deviates from the fitted curve for 20Mn-NC-second catalyst, which may be due to a weak Mn-O scattering path caused by a very small amounts of O, since MnPc does not have a Mn-O scattering path. We have attempted to add a Mn-O scattering path directly from the MnO

10

structure, but this did not provide us with representative structure information, suggesting that the real coordination of the Mn in the 20Mn-NC-second catalysts is complicated. As compared to standard MnPc that has a well-defined and uniform MnN_4 molecule structure, the 20Mn-NC-second catalyst exhibits disorganized structures especially in terms of the disordered nature and defective structures that comprise the edges of carbon planes and grain/domain boundary at the surface of the carbon particles. Due to a somewhat low content of Mn and a more disorganized, defective carbonaceous/meso-graphitic structure, the EXAFS data of the actual catalyst 20Mn-NC-second exhibits more noise, which could also contribute to the peak deviation observed at around 1.9 Ångstrom. We also compared the Mn catalysts at different synthesis stages, which shows the evolution of the Mn local structures and demonstrates the formation of atomically dispersed Mn sites instead of Mn clusters. Although we tried the XAS measurement for 20Mn-NC-first to study the possible structure changes of the active sites before and after the adsorption step during catalyst synthesis process. Due to a very low Mn concentration (0.68 wt.% by ICP-MS), the recorded spectrum was not sufficient for high quality data analyses (Supplementary Fig. 7).

The MnN_4 sites and their local carbon structures were further analyzed using X-ray photoelectron spectroscopy (XPS). The elemental quantifications from XPS data determined for the different precursors and Mn-N-C catalysts is summarized in Supplementary Table 5. The content of N in the 20Mn-ZIF precursor is 31.2 at.% and the N 1s spectrum shows a symmetric and sharp peak at 398.6 eV corresponding to C=N of 2-methylimidazole (**Fig. 2d**).[53] After

pyrolysis, the hydrocarbon networks of the ZIF precursors transformed into partially graphitized carbon with a N content of 2.2 at. %.[54] XPS data acquired from the samples obtained at the different processing steps exhibited nearly identical C 1s spectra (**Fig. 2e** and Supplementary Table 6) and carbon content, indicating that the second adsorption step does not induce any change to the carbon structure. Although the N content continuously decreased during processing to a level of 1.3 at. % after the second adsorption step, the amount of N appears to be sufficient to form a significant fraction of MnN_4 coordination relative to the low content of Mn (approximately half that of N). High-resolution N 1s XPS spectra further indicate that the two dominant peaks at 401.1 and 398.4 eV correspond to graphitic- and pyridinic-N, respectively, and the peak at 399.1 eV could be attributed to N atoms bonded to M sites,[55] likely MnN_4 in the catalysts. The percentage of MnN_4 increased from 5.8% to 11.2% after the second adsorption step (Supplementary Table 7); the percentage of pyridinic-N decreased by about 10%, likely due to further coordination with Mn ions as evidenced by the N 1s peak shift from the original pyridinic-N at 398.4 eV to 399.1 eV. Overall, the total nitrogen content loss does not lead to a decline in activity, suggesting that the chemical state of N is more important than the total N content. Generally, graphitic-N atoms modify the electronic structure, while pyridinic-N ones serve as coordination sites with M ions.[40] The XPS Mn 2p peak of 20Mn-NC-first (**Fig. 2f**) shows a 0.7 eV shift to a higher bonding energy compared with the sample before acid leaching (20Mn-NC). It has been reported that the interaction between metallic clusters and $M-N_x$ can change the charge density of the central metal ions and leads to a shift in the binding energy.[17] Thus, the positive shift may be due to the removal of Mn clusters during acid leaching.

Considering that 20Mn-NC-first and 20Mn-NC-second exhibit the same Mn 2p peak position, no additional Mn clusters are produced during the second adsorption step, which is in good agreement with XAS and XRD analyses.

Fig. 3a-c present typical bright field (BF) and medium-angle annular dark field (MAADF) STEM images of the carbon particles in the 20Mn-NC-second catalyst that show highly disordered carbon structures with randomly oriented graphitic domains and less dense, pore-like (dark contrast in Fig. 3c). Similar morphologies were observed in other ZIF-8-derived catalysts,[32,40,41] but the Mn-N-C catalyst appears to contain the domains with higher degree of graphitization. Low voltage, aberration-corrected STEM imaging coupled with EELS was used to study the atomic dispersion and local environment of Mn at an atomic resolution. The MAADF detector extends the range of the collection semi-angle to 54-200 mrad (*vs.* 86-200 mrad for HAADF), which can provide more contrast from lower-scattering, light elements *e.g.*, carbon. Distinguishable signals for C, N, O, and Mn are observed in the EELS maps across the carbon nanoparticles (**Fig. 3e-h**), respectively, acquired for the particle shown in Fig. 3d. The bright spots shown in the high-resolution MAADF-STEM images in **Fig. 3i, j** correspond to single heavy atoms that are uniformly dispersed across/within the carbon structure, indicating a high density of Mn-doping. Furthermore, an EEL point spectrum (**Fig. 3k**) was obtained by placing the 1 Ångstrom electron probe directly on a single atom (*e.g.*, as circled in red in **Fig. 3j)**, which are near the edge of a single or double graphene layer (basal planes) that form the graphite domains of the carbon naoparticles. Based on the Å resolution of the electron probe and thin

sample area, the signal that contributes to the EEL point spectrum (Fig 3k) originates from the atom and its closest neighboring atoms. The co-existence of N and a single Mn within this Å-region provides strong evidence for a Mn-N coordinate structure, suggesting that the single Mn ions are anchored by N within carbon. The immediate vicinity of single Mn sites with N is confirmed by similar EELS analyses acquired from different areas of the catalysts (Supplementary Fig. 8).

Importantly, atomically dispersed Mn sites are also observed in MAADF-STEM images acquired of the 20Mn-NC-first catalyst and the EEL point spectra reveal a similar co-existence of Mn and N (Supplementary Fig. 8). We infer from this result that the state of Mn in the 20Mn-NC-fisrt is similar to that in the 20Mn-NC-second, and is likely that of a MnN_4 coordinated structure. The primary difference between the two catalysts is that the density of MnN_4 active sites is significantly increased after the second adsorption step. The signals of both Mn and N become much stronger after the second adsorption step as evidenced in the comparison of the EELS elemental maps (Supplementary Fig. 9), indicating a higher density of MnN_4, which is also verified by MAADF-STEM imaging, as shown in Supplementary Fig. 8. Although a number of bright spots are uniformly dispersed in the MAADF-STEM images for 20Mn-NC-first, only a few Mn-N coordinated sites were confirmed by EELS. Many of the brighter atoms probed showed N but not Mn by EELS and may be residual Zn (0.1 at. %, Supplementary Table 5). After the second adsorption step, the co-existence of Mn and N becomes dominant and is easily verified by EEL spectra acquired for many different areas,

14

indicating a significant increase in the density of MnN$_4$ sites in the 20Mn-NC-second catalyst. Inductively coupled plasma-mass spectroscopy (ICP-MS) results also verify that the Mn content increases from 0.68 wt. % in the 20Mn-NC-first to 3.03 wt. % in the 20Mn-NC-second. Gradually increasing the density of MnN$_4$ active sites without forming Mn clusters/aggregates is critically important for activity enhancement. In the case of Fe-N-C catalysts, an efficient one-step method has been explored by Jaouen *et al*. to obtain a high density of atomically dispersed FeN$_4$C$_{12}$ active sites.[40,56] However, such processing has not successfully been transferred to the Mn system, because it is very easy to form oxides clusters and aggregates even at a relatively low Mn content during the pyrolysis step. The two-step Mn doping-adsorption method effectively increases the density of MnN$_4$ active sites without the concomitant formation of Mn-oxides clusters, thereby achieving an exceptionally enhanced catalytic activity.

ORR activity of atomically dispersed Mn-N-C catalysts. The ORR activity and four-electron selectivity (H$_2$O$_2$ yield) of all catalyst samples were evaluated by using a rotating ring-disk electrode (RRDE) in a 0.5 M H$_2$SO$_4$ electrolyte. Unlike ZIF-derived Fe and Co catalysts, one-step chemical doping of Mn into ZIFs is not an effective method to generate high ORR activity. With Mn doping content ranging from 0 to 30 at. %, poor ORR activity is measured for all Mn-NC-first samples exhibiting $E_{1/2}$ less than 0.65 V, which is likely due to an insufficient density of active sites (Supplementary Fig. 10). Thus, inspired by the concept of host-guest strategy,[48] we introduced more MnN$_4$ active sites into the promising Mn-NC-first host by conducting the second adsorption step. As shown in **Fig. 4a**, after the second adsorption step,

both Mn-free (0Mn-NC) and 20Mn-NC catalysts showed significantly enhanced activity with the 20Mn-NC-second catalyst exhibiting the most positive $E_{1/2}$ up to 0.8 V *vs*. RHE. Note that there is no Fe contamination during this multi-step processing procedure, as evidenced by negligible Fe content in the catalysts determined by ICP-MS and XPS analyses (Supplementary Fig. 11) as well as poor activity of the Mn-free control sample after multiple heating treatments. Considering the comparable carbon structure and N dopant (Supplementary Table 1 and 5) before and after the adsorption step of synthesis, the enhanced performance was originated from the increasing MnN_4 concentration. Poisoning experiment was performed by employing KSCN to block the M-N$_x$ sites.[57] The negative shift of 150 mV of $E_{1/2}$ (Supplementary Fig. 12) further verifies that the primary active sites in the 20Mn-NC-second catalyst are metal-based MnN_4, instead of metal-free CN_x sites. The ORR activity is therefore proportional to the MnN_4 concentration, and the key to further improving catalyst activity is to create more atomically dispersed MnN_4 sites in carbon matrix without the formation of clusters. To further verify the effectiveness of the second adsorption step, an identical adsorption step was performed using commercial carbon black (ketjenblack-KJ-black) and polyaniline-derived nanocarbon (PANI-NC). The adsorption step leads to an obvious enhancement of activity for both KJ-black and PANI-NC (**Fig. 4b**), indicating that the adsorption step is an effective strategy to introduce MnN_4 active sites, regardless of the carbon host. The activity of the ZIF derived 0Mn-NC-first, however, is much higher than that for either KJ-black and PANI-NC, which supports that an optimal nitrogen doping level and the pore structure of the carbon host are crucial parameters during the adsorption step. Furthermore, we studied the effect of the nitrogen source used for

16

adsorption (**Fig. 4c** and Supplementary Fig. 13) on catalytic activity and find that adsorption using distinct Mn salts without N source still leads to an improvement in the activity. This suggests that Mn ions could be chemically bonded with the pre-doped N in the carbon structure and form active sites through subsequent thermal activation. Co-adsorption of Mn and N sources yield improved activity with an increased N content in the final catalyst (20Mn-NC-second) as evidenced by XPS (Supplementary Table 5). Due to significantly reduced micropores and BET surface areas of the carbon host after adsorption process (Supplementary Fig. 14), we believe that N-sources can stabilize Mn ions through possible coordination in the micropores of the carbon host. During the pyrolysis, the N source creates additional N doping in the carbon host, which can further coordinate with Mn species and form MnN_4 active sites. Cyanamide as a N-source exhibited the best performance, compared to other N-sources (*e.g.*, dipicolylamine, phenanthroline, and melamine), probably due to its size and/or unique $C\equiv N$ structures. The $C\equiv N$ structures decompose at the elevated temperature and easily bond to unsaturated carbon atoms to form thermodynamically stable pyridinic-N.[49] This is favorable for the formation of MnN_4 active sites. Excess defects, such as those created by heteroatom dopants in catalysts can compromise the electrical conductivity of carbon materials, and reduce the overall performance. During the second adsorption step, however, the introduction of defects via N- and Mn- doping are critical to form a high density of MnN_4 active sites, compared to the any negative influence on the electrical conductivity because of their relatively low doping content.

The influence of post-treatments on the Mn-NC host before adsorption was investigated. When directly using 20Mn-NC without an acidic treatment as the host for the second adsorption step, the activity showed an obvious decline (Supplementary Fig. 15a). Since the acid leaching step is associated with the removal of Mn clusters, it is not a crucial step when using the Mn-free 0Mn-NC host for adsorption (Supplementary Fig. 15b). Acid leaching effectively removes the MnO clusters from 20Mn-NC, which likely opens or creates pore structures, thus increasing micropore sizes (from 1.0 to 1.4 nm) and surface areas (from 699 to 821 m^2/g) (Supplementary Fig. 16 and Supplementary Table 8). The acidic leaching conditions were found nearly no influence on catalyst activity when the concentration of H_2SO_4 is higher than 0.2 M (Supplementary Fig. 17). The electrochemically accessible surface area (EASA) of the catalysts were estimated based on their cyclic voltammetry (CV) curves in N_2 saturated 0.5 M H_2SO_4 (Supplementary Fig. 18). The 20Mn-NC-second catalyst exhibits the highest EASA of 715 m^2/g (Supplementary Table 9), which is favorable for exposing more active sties. In spite of its high EASA of 660 m^2/g, the ORR activity of 0Mn-NC-second is disappointing, indicating a lower density of active sites in the catalyst. N_2 adsorption-desorption isotherms were analyzed to study the BET surface areas and pore-size distributions of the different catalysts (Supplementary Fig. 19 and Supplementary Table 8). Pre-doping of Mn in ZIF precursors is crucial for subsequent adsorption because it enables the catalysts to maintain sufficiently microporous structures. Doping of 20 at.% Mn is found to be optimal; however, excess doping of Mn (*e.g.*, 30 at. %) results in a low surface area (245 m^2/g) even after acidic leaching. The correlation between the porous structure of the carbon host and the ORR activity was established (Supplementary Fig. 20)

and reveals that the final activity depends significantly on the structure of the host used for the adsorption step.

The ORR activity of the best performing 20Mn-NC-second catalyst is higher than for a 20Co-NC-second catalyst and approaches that of a 20Fe-NC-second catalyst (**Fig. 4d**), which is only 60 mV less than of a commercial Pt/C catalyst (~0.86 V). The onset potential is comparable to that of the 20Fe-NC-second catalysts (*c.a.* 0.96 V), indicating a similar intrinsic activity between MnN_4 and FeN_4 sites for the ORR in acidic media. Thus, atomically dispersed single Mn site catalyst represents the best activity for Mn-N-C catalysts as well as for other Fe-free catalysts (Supplementary Table 10).[58] Importantly, the H_2O_2 yield of the 20Mn-NC-second catalyst is less than 2% indicating a $4e^-$ reduction pathway, which is comparable to 20Fe-NC-second, and much lower than that of 20Co-NC-second (**Fig. 4e**). Moreover, when the catalyst loadings vary within a wide range from 0.2 to 1.2 mg/cm^2, the H_2O_2 yields (Supplementary Fig. 21) remain at a very low level (<4%). This further proves that the $4e^-$ pathway of O_2 is dominant on 20Mn-NC-second, rather than the $2e^-+2e^-$ pathway. A Tafel slope of ~80 mV/dec for the best performing 20Mn-NC-second is comparable to that of Co- or Fe-based catalysts (Supplementary Fig. 22 and Supplementary Table 11), indicating a similar rate-determining step involving mixed controls including transfer of the first electron (118 mV/dec) and the diffusion of intermediates at catalyst surfaces (59 mV/dec).[59]

The best performing 20Mn-NC-second catalyst is further studied as a cathode in membrane-electrode-assemblies (MEAs) for fuel cells. The open circuit voltage (OCV) is as

19

high as 0.95 V using H_2 and O_2, which is in good agreement with the ORR onset potential determined using RDE. The fuel cell performance using the 20Mn-NC-second as the cathode catalyst is very encouraging an is capable of generating current densities of 0.35 and 2.0 A/cm^2 at 0.6 and 0.2 V, respectively, in H_2/O_2 at a reasonable 1.0 bar partial pressure (**Fig. 4f**). The corresponding power density is up to 0.46 W/cm^2. The achieved performance exceeds the Fe-N-C catalyst derived from PANI reported in 2011;[60] however, the performance is inferior to the two-step 20Fe-N-C catalyst, especially in the kinetic range, which agrees with RDE tests in a 0.5 M H_2SO_4 electrolyte.

Enhanced catalyst stability in acids. The stability of the best performing 20Mn-NC-second catalyst was studied using both accelerated stress tests (ASTs) by potential cycling (0.6-1.0 V) and chronoamperometry at constant potentials ($E = 0.7$ and 0.8 V) in O_2-saturated 0.5 M H_2SO_4. The 20Mn-NC-second catalyst exhibited excellent stability, as evidenced by a loss of only 17 mV in $E_{1/2}$ after 30,000 potential cycles (**Fig. 5a**). The stability is enhanced over traditional Fe-N-C catalysts derived from PANI (loss 80 mV after 5000 cycles),[60] as well as the ZIF-derived 20Fe-NC-second catalyst (29 mV loss after 30,000 cycles) (**Fig. 5b**). After the potential cycling ASTs, the microstructure and morphology of carbon phases in the 20Mn-NC-second catalyst remain nearly the same (Supplementary Fig. 23), which is in good agreement with the enhanced corrosion resistance of the carbon derived from Mn-ZIF-8 precursors. Furthermore, long-term durability tests were conducted by holding at a constant potential of 0.7 V for 100 hours in O_2-saturated 0.5 M H_2SO_4 (**Fig. 5c**). The 20Mn-NC-second catalyst retains 88% of its initial

current density and exhibits a 29 mV loss of $E_{1/2}$ after 100 hours (**Fig. 5d**). The identical CVs before and after the stability tests (inset of **Fig. 5d**) indicate excellent resistance to carbon corrosion. To test the 20Mn-MC-second catalyst under even harsher conditions, we performed the durability test at 0.8 V (**Fig. 5e**). A larger decline of the current density of 57% after 100 hours is observed at 0.8 V, relative to 0.7 V. Interestingly, the loss of current density during the test can be partially recovered by potential cycling between 0 to 1.0 V. For the first 20 hours, nearly 90% of the activity can be restored. However, the irreversible loss accumulates and the current density only recovers 70% after 80 hours, indicating that the activity loss is due to multiple factors, including irreversible and reversible degradation. The reversible activity loss may be associated with deactivation of active sites by anion binding or reversible adsorption of oxygen-containing functional groups on local carbon atoms adjacent to MnN_4 sites, which are considered to be part of the active sites.[61] After the 100-hour test at 0.8 V, $E_{1/2}$ showed a loss of 18 mV for the 20Mn-NC-second catalyst (**Fig. 5f**). In comparison, the 20Fe-NC-second catalyst only retains 39% of its activity, although similar activity recovery is observed, and a loss of $E_{1/2}$ is up to 48 mV after 100 hours at 0.8 V (Supplementary Fig. 24). The CV changes for the 20Mn-NC-second catalyst (**inset of Fig. 5f**) is around 30%, much less than that of the 20Fe-NC-second catalyst (60%), suggesting an enhanced carbon oxidation-resistance for the Mn catalyst. Note that the current densities for 20Mn-NC-second and 20Fe-NC-second catalysts are different at 0.8 V. The catalyst degradation may be dependent on total number of electrons passing through catalysts during the ORR. Therefore, we calculated the degradation rates against the total electric charge by integrating the i-t curve (Supplementary Table 12). In the case of the

20Mn-NC-second catalyst, the degradation of $E_{1/2}$ at 0.8 V is 0.237 mV/C, much less than that for the 20Fe-NC-second catalyst (0.716 mV/C). Stability tests conducted at a constant current density (1.42 mA/cm^2) further verified that the 20Mn-NC-second catalyst is more stable than the 20Fe-NC-second catalyst (Supplementary Fig. 25). In addition to the possible intrinsic stability of MnN$_4$ *vs*. FeN$_4$, the enhanced stability of the Mn-N-C catalyst likely results from the improved corrosion-resistance of the carbon derived from Mn-doped ZIF-8 precursors. Corrosion-resistance of carbon in catalysts was further assessed by cycling at a high potential range (1.0-1.5 V) in N$_2$-saturated 0.5 M H$_2$SO$_4$ (Supplementary Fig. 26). After 5000 AST cycles, the EASAs of the 20Mn-NC-second and 30Mn-NC-second increase 52% and 34%, respectively, suggesting carbon oxidation in catalysts. However, these values are much less than those of 0Mn-NC-second (70%) and the 20Fe-NC-second catalyst (94%) (Supplementary Table 9), indicating significantly enhanced carbon stability due to Mn doping into ZIF-8 precursors.

To evaluate catalyst stability under real fuel cell operating conditions, we conducted 100-hour life tests at a challenging high voltage of 0.7 V for MEAs made with the 20Mn-NC-second catalyst (Supplementary Fig. 27). Although an initial degradation occurred at 0.7 V, enhanced durability of the Mn-N-C cathode was observed, when compared to Co and Fe-based catalysts.[26,32] In addition to the intrinsic stability of the 20Mn-NC-second catalysts, non-electrochemical factors including degradation of the catalyst/ionomer interfaces and water flooding also influence the performance durability of PGM-free cathodes in fuel cells. Due to carbon corrosion and dissolution of metal sites, current PGM-free catalysts suffer from rapid

degradation at relatively high potentials (>0.6 V).[26] The Mn-N-C catalyst prepared from the two-step doping and adsorption approach demonstrate encouraging stability and represent one of the most stable PGM-free catalysts in acidic electrolytes (Supplementary Table 10).

Density functional theory (DFT) calculations. To gain a fundamental understanding of the origin of the catalytic activity for the atomically dispersed and N coordinated single Mn site catalysts, first principles DFT calculations were performed. A variety of metal-free active sites associated with nitrogen dopings and carbon defects have been extensively studied before by using the first-principles calculations in terms of their ORR activity such as pyrrolic nitrogen, pyridinic nitrogen, graphitic nitrogen at both edge and bulk, five-carbon ring, seven-carbon ring, and five-carbon ring adjacent to seven-carbon ring.[62] Due to the significant difference of ORR mechanisms in alkaline and acidic media, those metal-free active sites are not effective to catalyze the ORR via a 4e$^-$ pathway in acidic media, while they exhibits good activity in alkaline media. Therefore, we focus on a variety of possible MnN_xC_y active sites and predict their adsorption energies, free energy evolution, and activation energies for the ORR in acids. As shown in Supplementary Fig. 28, nine possible active sites (denoted as MnN_2C_{12}, MnN_3C_9, MnN_3C_{11}, MnN_4C_8, MnN_4C_{10}, MnN_4C_{12}, MnN_5C_{10}, $Mn_2N_5C_{12}$, and $Mn_2N_6C_{14}$) are carefully examined in the computational study. The predicted adsorption energy of O_2, OOH, O, OH, and H_2O on each of these potential MnN_xC_y active sites are presented in Supplementary Table 13. The DFT adsorption energy results indicate that MnN_2C_{12} and MnN_3C_9 sites, which have fewer chelated N atoms around the central metal atom than the other sites, bind the final product H_2O

23

too strongly to be good ORR active sites. Moreover, MnN_3C_{11}, MnN_4C_8, and $Mn_2N_5C_{12}$ sites are predicted to bind the ORR intermediate OH too strongly, which are also not good ORR active sites as well. Computational screening identified that MnN_4C_{10}, MnN_4C_{12}, MnN_5C_{10}, and $Mn_2N_6C_{14}$ sites have an appropriate binding strength with the ORR species and can be active sites for the 4e⁻ ORR.

Based on XAS analyses, which suggest that MnN_4 structures are likely. Among studied MnN_4C_y sites, the MnN_4C_{12} site (a Mn-N_4 moiety bridging over two adjacent zigzag graphitic edges, as shown in **Fig. 6a**) was further predicted as the most optimal active sites (Supplementary Table 13). Its calculated free energy evolution for the ORR (**Fig. 6b**) and the transition state for an OOH dissociation on the active site were also studied (**Fig. 6c**). We assumed a 4e⁻ ORR pathway, in which an O_2 molecule will first adsorb on the top of central Mn and, then O_2 will be pronated to form OOH. Next, the OOH will dissociate into O and OH, and finally both O and OH will be pronated to form the final product H_2O. We employed the computational hydrogen electrode method developed by Nørskov *et al.*[63] and computed the free energies of all elementary steps as a function of electrode potential U with reference to the reversible hydrogen electrode (RHE). Fig. 6b shows that, under the standard potentials of the ORR, U = 1.23 V, *i.e.* zero overpotential, some of the elementary reactions along the 4e- ORR associative pathway are endergonic and thus thermodynamically unfavorable on the MnN_4C_{12} site. However, the free energy change for these elementary reactions involving charge-transfer will become negative (*i.e.*, exergonic reaction) when the electrode potential U is lower than a

limiting potential of 0.80 V. Moreover, our computational results shwon in **Fig. 6b** show that both the free energy differences between O_2* and OOH* as well as between OH* and H_2O* (* represents the adsorption of the molecule on the active site) are close to zero under the limiting potential, suggesting that the MnN_4C_{12} site could have an optimal activity for the ORR.[64] We performed the climbing image nudged elastic band (CI-NEB) calculation to locate the transition state and predict the activation energies for the OOH dissociation reaction,[65] which is the crucial step of breaking the O-O bond for the 4e- ORR associative pathway on the MnN_4C_{12} site. **Fig. 6c** shows the atomic details of this reaction. In the initial state, OOH is adsorbed on the central Mn atom; in the final state, both the dissociated O and OH are co-adsorbed on the central Mn atom. The reaction process from the initial state to the final state requires passing a transition state and overcoming an energy barrier of 0.49 eV, which is surmountable. Consequently, the DFT results predict that it is both thermodynamically and kinetically favorable for the 4e- ORR to occur on the MnN_4C_{12} site, which very likely exist in the atomically dispersed and nitrogen-coordinated Mn-N-C catalyst. It should be noted that our theoretical model of MnN_4C_{12} active site agrees with previous characterization studies on Fe- or Co- and N-doped carbon, in which FeN_4 and CoN_4 moieties are found to be the ORR active sites, respectively.[32,40,41,56,66] According to the XANES and EXAFS analysis (Figure 2), the atomic Mn sites in the catalysts have an oxidation state of 2+ and coordinated with N mainly in the form of MnN_4. The MAADF-STEM images (Figure 3) further proved the atomic dispersion and the detection of N immediate vicinity of the single Mn sites by EEL point spectrum. It provided strong evidence that Mn atoms were anchored by doped N. Hence, the computational model explains well our experimental findings.

Although multiple possible sites in nanocarbon are able to coordinate with single metals sites,[67] their ORR activities and stabilities in acids are not sufficient. In contrast, the MN_4 structure therefore is the most stable and the most active sites for the ORR in acids. The stable structure is due to the lone pair electrons in pyridinic-N, which can form strong coordination bonds with transition metals. In contrast, other defects like edge carbons cannot form stable bond with metal ions. Especially at high temperature, metal ions (not chelated with pyridinic N) will be reduced to zero valence by adjacent carbon atoms.[16,68]

We also performed DFT calculations to specifically examine the influence of water solvent on the ORR in Mn-N-C catalysts (Supplementary Fig. 29). Although the value of the limiting potential for the ORR active sites to be activated varies with the addition of a water layer, the same four-electron OOH dissociation pathway is still functional on the MnN_4C_{12} site. Consequently, the present computational study suggests that the water solvent effect is not significant enough to alter the reaction mechanism for the ORR on the Mn-N-C catalysts. In addition, the MnN_4 sites with surrounding graphitic-N dopants would also be active to promote the $4e^-$ ORR following the same OOH dissociation pathway (Supplementary Fig. 30). We predicted that the MnN_4 site with immediately adjacent graphitic-N dopants could have a lower limiting potential and lower activation energy for O-O bond breaking than the MnN_4 site without graphitic-N dopants. These DFT results strongly suggest that graphitic-N could improve the ORR activity of the MnN_4 site and hence could be beneficial for future Mn-N-C catalyst design and synthesis.

Conclusions

In summary, a new type of atomically dispersed and nitrogen-coordinated Mn-N-C catalyst was developed to address the performance degradation challenge that current Fe-N-C catalysts suffer from, especially due to harmful Fenton reactions present in fuel cell cathodes. Superior activity and enhanced stability in acidic media make the Mn-N-C catalyst a promising PGM-free and also Fe-free cathode for future PEMFC applications. Atomically dispersed MnN_4 sites were verified, for the first time, using XAS experiments to determine their possible coordination along with directly observed at the atomic scale using low voltage, aberration-corrected STEM imaging coupled with EELS analysis. An innovative two-step doping and adsorption approach was developed and proved effective to significantly increase the density of active sites. In the first step, an optimal Mn content was pre-doped into ZIFs during the nanocrystal growth followed by a carbonization and acidic leaching treatments. The doping of Mn not only helps to stabilize the carbon structure with high degree of graphitization, but also influences the formation of a favorable porous structures for the second adsorption step using additional Mn and N sources. The confinement strategy in the second adsorption step will be effective to generate additional MnN_4 sites without the formation of Mn aggregates. The high activity was evidenced by a commendable half-wave potential of 0.80 V *vs*. RHE in acids, which results from intrinsic activity of atomically dispersed MnN_4 sites with increased density within a 3D porous ZIF-derived carbon. The remarkable stability is due to the robust MnN_4 sites and the enhanced corrosion resistance of adjacent carbon derived from Mn doping. DFT calculations also further confirmed that MnN_4 sites possess comparable activity to FeN_4. Among the various possible MnN_xC_y sites, the MnN_4C_{12} site has a favorable binding energy with O_2, OOH, and H_2O during

the ORR as well as a surmountable energy barrier to break O-O bonds for complete 4e⁻ reduction. Therefore, the reported atomically dispersed Mn-N-C catalyst demonstrates a novel concept to develop robust and highly active PGM-free catalysts as replacements for Fe catalysts in future PEMFC technologies.

Acknowledgements

Author Contributions.

G.W., Z.W., and J. L. designed the experiments, analyzed the experimental data, and wrote the manuscript. J. L., M. C., and H. Z. synthesized catalyst samples and carried out electrochemical measurements. D.A.C., K.L.M, S.H., and D.S performed electron microscopy analyses and data interpretation. S. K. conducted XPS analysis. M.W., M.L., G.E.S., and Z.F. recorded and analyzed XAS data. C.L. and H.X. carried out fuel cell tests. B.L., K.L., and G.F.W. conducted computational studies.

References

1   Lefèvre, M., Proietti, E., Jaouen, F. & Dodelet, J.-P. Iron-based catalysts with improved oxygen reduction activity in polymer electrolyte fuel cells. *Science* **324**, 71-74, (2009).

2   Proietti, E. *et al.* Iron-based cathode catalyst with enhanced power density in polymer electrolyte membrane fuel cells. *Nat. Commun.* **2**, 416, (2011).

3   Wu, G. & Zelenay, P. Nanostructured nonprecious metal catalysts for oxygen reduction reaction. *Acc. Chem. Res.* **46**, 1878-1889, (2013).

4   Zhu, Y. P., Guo, C., Zheng, Y. & Qiao, S. Z. Surface and interface engineering of noble-metal-free electrocatalysts for efficient energy conversion processes. *Acc. Chem. Res.* **50**, 915-923, (2017).

5   Gewirth, A. A., Varnell, J. A. & DiAscro, A. M. Nonprecious metal catalysts for oxygen reduction in heterogeneous aqueous systems. *Chem. Rev.* **118**, 2313-2339, (2018).

6   Wu, G. Current challenge and perspective of pgm-free cathode catalysts for pem fuel cells. *Front. in Energy* **11**, 286-298, (2017).

7   Yan, D. *et al.* Defect chemistry of nonprecious-metal electrocatalysts for oxygen reactions. *Adv. Mater.* **29**, (2017).

8   Gong, K., Du, F., Xia, Z., Durstock, M. & Dai, L. Nitrogen-doped carbon nanotube arrays with high electrocatalytic activity for oxygen reduction. *Science* **323**, 760-764, (2009).

9   Donghui Guo, R. S., Chisato Akiba, Shunsuke Saji, Takahiro Kondo, Junji Nakamura. Active sites of nitrogen-doped carbon materials for oxygen reduction reaction clarified using model catalysts. *Science* **351**, 361-365, (2016).

10   Dai, L., Xue, Y., Qu, L., Choi, H. J. & Baek, J. B. Metal-free catalysts for oxygen reduction reaction. *Chem. Rev.* **115**, 4823-4892, (2015).

11   Zhang, J. & Dai, L. Heteroatom-doped graphitic carbon catalysts for efficient electrocatalysis of oxygen reduction reaction. *ACS Catal.* **5**, 7244-7253, (2015).

12   Masa, J., Xia, W., Muhler, M. & Schuhmann, W. On the role of metals in nitrogen-doped carbon electrocatalysts for oxygen reduction. *Angew. Chem. Int. Ed.* **54**, (2015).

13   Yu, D., Zhang, Q. & Dai, L. Highly efficient metal-free growth of nitrogen-doped single-walled carbon nanotubes on plasma-etched substrates for oxygen reduction. *J. Am. Chem. Soc.* **132**, 15127-15129, (2010).

14   Wu, G., More, K. L., Johnston, C. M. & Zelenay, P. High-performance electrocatalysts for oxygen reduction derived from polyaniline, iron, and cobalt. *Science* **332**, 443-447, (2011).

15   Jaouen, F. *et al.* Recent advances in non-precious metal catalysis for oxygen-reduction reaction in polymer electrolyte fuelcells. *Energy Environ. Sci.* **4**, 114-130, (2011).

16   Liu, J. *et al.* High performance platinum single atom electrocatalyst for oxygen reduction reaction. *Nat. Commun.* **8**, 15938, (2017).

17   Jiang, W. J. *et al.* Understanding the high activity of fe-n-c electrocatalysts in oxygen reduction: Fe/fe3c nanoparticles boost the activity of Fe-$N_{(x)}$. *J. Am. Chem. Soc.* **138**, 3570-3578, (2016).

18   Tang, C. & Zhang, Q. Nanocarbon for oxygen reduction electrocatalysis: Dopants, edges, and defects. *Adv. Mater.* **29**, (2017).

19   Yu, H. *et al.* Nitrogen-doped porous carbon nanosheets templated from g-C_3N_4 as metal-free electrocatalysts for efficient oxygen reduction reaction. *Adv. Mater.* **28**, 5080-5086, (2016).

20   Li, J. *et al.* S, n dual-doped graphene-like carbon nanosheets as efficient oxygen reduction reaction electrocatalysts. *ACS Appl. Mater. Interfaces* **9**, 398-405, (2017).

21   Ahmed, M. S. & Kim, Y.-B. Amide-functionalized graphene with 1,4-diaminobutane as efficient metal-free and porous electrocatalyst for oxygen reduction. *Carbon* **111**, 577-586, (2017).

22   Sun, T., Tian, B., Lu, J. & Su, C. Recent advances in Fe (or Co)/N/C electrocatalysts for the oxygen reduction reaction in polymer electrolyte membrane fuel cells. *J. Mater. Chem. A* **5**, 18933-18950, (2017).

23   Yan, X. *et al.* Atomic interpretation of high activity on transition metal and nitrogen-doped carbon nanofibers for catalyzing oxygen reduction. *J. Mater. Chem. A* **5**, 3336-3345, (2017).

24   Sa, Y. J. *et al.* A general approach to preferential formation of active fe-nx sites in fe-n/c electrocatalysts for efficient oxygen reduction reaction. *J. Am. Chem. Soc.* **138**, 15046-15056, (2016).

25   Banham, D. *et al.* A review of the stability and durability of non-precious metal catalysts for the oxygen reduction reaction in proton exchange membrane fuel cells. *J. Power Sources* **285**, 334-348, (2015).

26   Ferrandon, M. *et al.* Stability of iron species in heat-treated polyaniline–iron–carbon polymer electrolyte fuel cell cathode catalysts. *Electrochim. Acta* **110**, 282-291, (2013).

27   Choi, C. H. *et al.* Stability of fe-n-c catalysts in acidic medium studied by operando spectroscopy. *Angew. Chem. Int. Ed.* **54**, 12753-12757, (2015).

28   Li, X., Liu, G. & Popov, B. N. Activity and stability of non-precious metal catalysts for oxygen reduction in acid and alkaline electrolytes. *J. Power Sources* **195**, 6373-6378, (2010).

29   Kramm, U. I., Lefevre, M., Bogdanoff, P., Schmeisser, D. & Dodelet, J. P. Analyzing structural changes of Fe-N-C cathode catalysts in pem fuel cell by mossbauer spectroscopy of complete membrane electrode assemblies. *J. Phys. Chem. Lett.* **5**, 3750-3756, (2014).

30   Goellner, V. *et al.* Degradation of Fe/N/C catalysts upon high polarization in acid medium. *Phys. Chem. Chem. Phys.* **16**, 18454-18462, (2014).

31   Walling, C. Fenton's reagent revisited. *Acc. Chem. Res.* **8**, 125-131, (1975).

32   Wang, X. X. *et al.* Nitrogen-coordinated single cobalt atom catalysts for oxygen reduction in proton exchange membrane fuel cells. *Adv. Mater.*, (2018).

33   Zhong, Y. *et al.* The constraints of transition metal substitutions (Ti, Cr, Mn, Co and Ni) in magnetite on its catalytic activity in heterogeneous fenton and uv/fenton reaction: From the perspective of hydroxyl radical generation. *Appl. Cataly. B Environ.* **150-151**, 612-618, (2014).

34   Wu, G. *et al.* Synthesis–structure–performance correlation for polyaniline–Me–C non-precious metal cathode catalysts for oxygen reduction in fuel cells. *J. Mater. Chem.* **21**, 11392-11405, (2011).

35   Watts, R. J., Sarasa, J., Loge, F. J. & Teel, A. L. Oxidative and reductive pathways in manganese-catalyzed fenton's reactions. *J. Environ. Eng.* **131**, 158-164, (2005).

36   Gupta, S. *et al.* Quaternary feconimn-based nanocarbon electrocatalysts for bifunctional oxygen reduction and evolution: Promotional role of mn doping in stabilizing carbon. *ACS Catal.* **7**, 8386-8393, (2017).

37   Wang, X. *et al.* Size-controlled large-diameter and few-walled carbon nanotube catalysts for oxygen reduction. *Nanoscale* **7**, 20290-20298, (2015).

38   Zhang, H., Osgood, H., Xie, X., Shao, Y. & Wu, G. Engineering nanostructures of pgm-free oxygen-reduction catalysts using metal-organic frameworks. *Nano Energy* **31**, 331-350, (2017).

39   Wu, G. *et al.* Carbon nanocomposite catalysts for oxygen reduction and evolution reactions: From nitrogen doping to transition-metal addition. *Nano Energy* **29**, 83-110, (2016).

40   Zhang, H. *et al.* Single atomic iron catalysts for oxygen reduction in acidic media: Particle size control and thermal activation. *J. Am. Chem. Soc.* **139**, 14143-14149, (2017).

41   Pan, F. *et al.* Unveiling active sites of CO_2 reduction on nitrogen-coordinated and atomically dispersed iron and cobalt catalysts. *ACS Catal.* **8**, 3116-3122, (2018).

42   Wang, X. X. *et al.* Ordered Pt_3Co intermetallic nanoparticles derived from metal–organic frameworks for oxygen reduction. *Nano Lett.* **18**, 4163-4171, (2018).

43   Wang, H., Zhu, Q.-L., Zou, R. & Xu, Q. Metal-organic frameworks for energy applications. *Chem* **2**, 52-80, (2017).

44   Yang, L., Zeng, X., Wang, W. & Cao, D. Recent progress in MOF-derived, heteroatom-doped porous carbons as highly efficient electrocatalysts for oxygen reduction reaction in fuel cells. *Adv. Func. Mater.* **28**, (2018).

45   Xia, B. Y. *et al.* A metal–organic framework-derived bifunctional oxygen electrocatalyst. *Nat. Energy* **1**, 15006, (2016).

46   Wang, J. *et al.* ZIF-8 with ferrocene encapsulated: A promising precursor to single-atom fe embedded nitrogen-doped carbon as highly efficient catalyst for oxygen electroreduction. *Small* **14**, 1704282 (2018).

47   Gu, W., Hu, L., Li, J. & Wang, E. Recent advancements in transition metal-nitrogen-carbon catalysts for oxygen reduction reaction. *Electroanalysis* **30**, 1217-1228, (2018).

48   Lai, Q. *et al.* Metal–organic-framework-derived Fe-N/C electrocatalyst with five-coordinated fe-nx sites for advanced oxygen reduction in acid media. *ACS Catal.* **7**, 1655-1663, (2017).

49   Zhang, C. *et al.* Unlocking the electrocatalytic activity of chemically inert amorphous carbon-nitrogen for oxygen reduction: Discerning and refactoring chaotic bonds. *ChemElectroChem* **4**, 1269-1273, (2017).

50   Zhao, C. *et al.* Ionic exchange of metal-organic frameworks to access single nickel sites for efficient electroreduction of CO_2. *J. Am. Chem. Soc.* **139**, 8078-8081, (2017).

51   Feng, Z. *et al.* Atomic-scale cation dynamics in a monolayer VO_x/α-Fe_2O_3 catalyst. *RSC Adv.* **5**, 103834-103840, (2015).

52   Weng, Z. *et al.* Active sites of copper-complex catalytic materials for electrochemical carbon dioxide reduction. *Nat. Commun.* **9**, 415, (2018).

53   Liu, Z. *et al.* Tuning the electronic environment of zinc ions with a ligand for dendrite-free zinc deposition in an ionic liquid. *Phys. Chem. Chem. Phys.* **19**, 25989-25995, (2017).

54   Zhao, J. *et al.* Hydrophilic hierarchical nitrogen-doped carbon nanocages for ultrahigh supercapacitive performance. *Adv. Mater.* **27**, 3541-3545, (2015).

55   Chen, Y. Z. *et al.* From bimetallic metal-organic framework to porous carbon: High surface area and multicomponent active dopants for excellent electrocatalysis. *Adv. Mater.* **27**, 5010-5016, (2015).

56   Zitolo, A. *et al.* Identification of catalytic sites for oxygen reduction in iron- and nitrogen-doped graphene materials. *Nat. Mater.* **14**, 937-942, (2015).

57   Wang, Q. *et al.* Phenylenediamine-based fen x/c catalyst with high activity for oxygen reduction in acid medium and its active-site probing. *J. Am. Chem. Soc.* **136**, 10882-10885, (2014).

58   Sahraie, N. R. *et al.* Quantifying the density and utilization of active sites in non-precious metal oxygen electroreduction catalysts. *Nat. Commun.* **6**, 8618, (2015).

59   Li, Y. *et al.* An oxygen reduction electrocatalyst based on carbon nanotube-graphene complexes. *Nat. Nanotech.* **7**, 394-400, (2012).

60   Wu, G. *et al.* Titanium dioxide-supported non-precious metal oxygen reduction electrocatalyst. *Chem. Commun.* **46**, 7489-7491, (2010).

61   Herranz, J. *et al.* Unveiling n-protonation and anion-binding effects on Fe/N/C-catalysts for o2 reduction in pem fuel cells. *J Phys. Chem. C* **115**, (2011).

62   Tang, C. *et al.* Topological defects in metal-free nanocarbon for oxygen electrocatalysis. *Adv. Mater.* **28**, 6845-6851, (2016).

63   Norskov, J. K. *et al.* Origin of the overpotential for oxygen reduction at a fuel-cell cathode. *J. Phys. Chem. B* **108**, 17886-17892, (2004).

64   Kulkarni, A., Siahrostami, S., Patel, A. & Norskov, J. K. Understanding catalytic activity trends in the oxygen reduction reaction. *Chem. Rev.* **118**, 2302-2312, (2018).

65   Henkelman, G., Uberuaga, B. P. & Jónsson, H. A climbing image nudged elastic band method for finding saddle points and minimum energy paths. *J. Chem. Phys.* **113**, 9901-9904, (2000).

66   Chung, H. T. *et al.* Direct atomic-level insight into the active sites of a high-performance pgm-free orr catalyst. *Science* **357**, 479-484, (2017).

67   Zhang, C., Zhang, W. & Zheng, W. Pinpointing single metal atom anchoring sites in carbon for oxygen reduction: Doping sites or defects? *Chin. J. Catal.* **39**, 4-7, (2018).

68   Zeng, M. *et al.* Metallic cobalt nanoparticles encapsulated in nitrogen-enriched graphene shells: Its bifunctional electrocatalysis and application in zinc–air batteries. *Adv. Func. Mater.* **26**, 4397-4404, (2016).
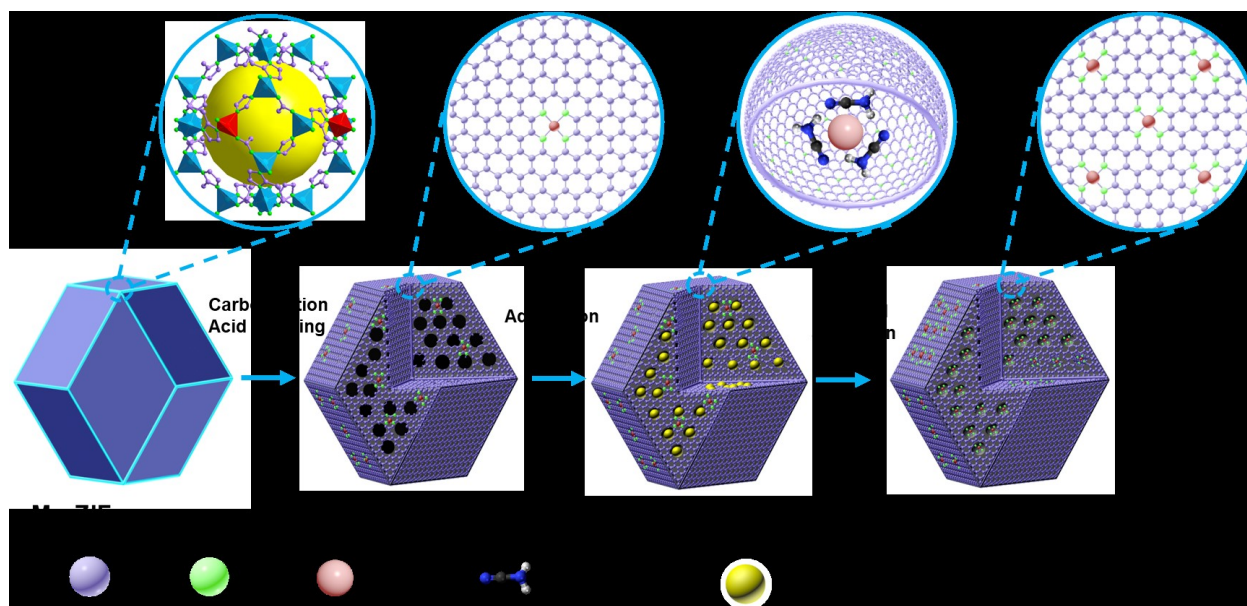
Fig. 1 | Schematic diagram of atomically dispersed MnN4 site catalysts. A two-step doping and adsorption approach can gradually increase the density of the atomically dispersed and nitrogen-coordinated MnN4 sites into the 3D carbon particles. In the first step, Mn-doped ZIF precursors are carbonized and then leached with an acid solution to prepare partially graphitized carbon host with unique nitrogen doping and microporous structures. In the second step, additional Mn and N sources were adsorbed into the 3D carbon host followed by a thermal activation to generate increased density of MnN4 active sites.
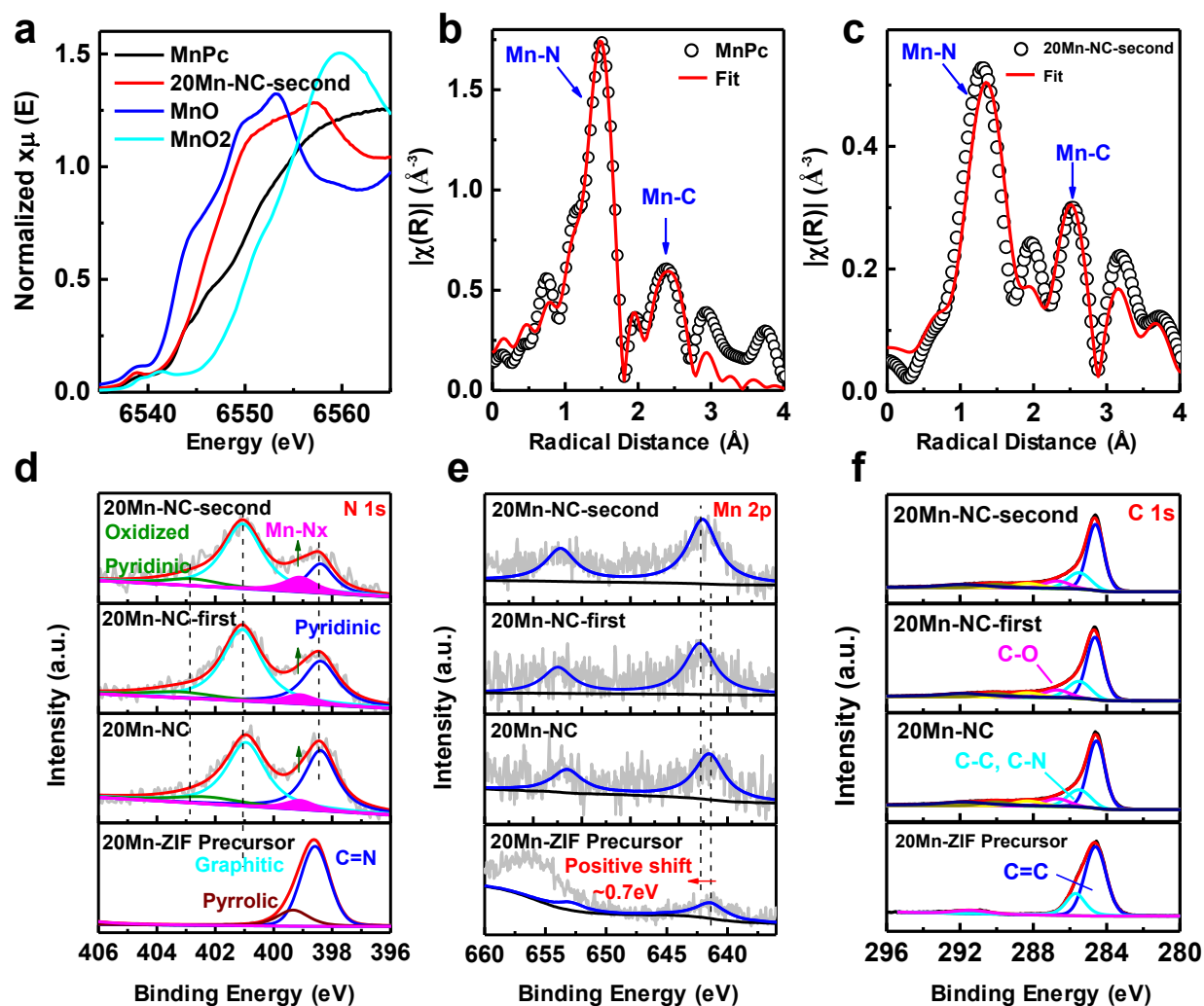
Fig. 2 | Structural characterization by XANES, EXAFS, and XPS. a, The experimental K-edge XANES spectra of 20Mn-NC-second catalyst and reference samples (MnO, MnO_2, and standard MnPc). **b,c,** Fourier transforms of Mn K-edge EXAFS data (open circle) and model-based fits (red line) of standard MnPc (**b**) and the 20Mn-NC-second (**c**). **d-f**, High-resolution N 1s (**d**), C 1s (**e**), and Mn 2p (**f**) XPS data of materials obtained from different processing steps. 20Mn-NC prepared through a pyrolysis of the 20Mn-ZIF precursor. 20Mn-NC-first obtained after an acid leaching and a heat treatment of 20Mn-NC. 20Mn-NC-second catalysts are final catalysts after two step doping and adsorption processes.
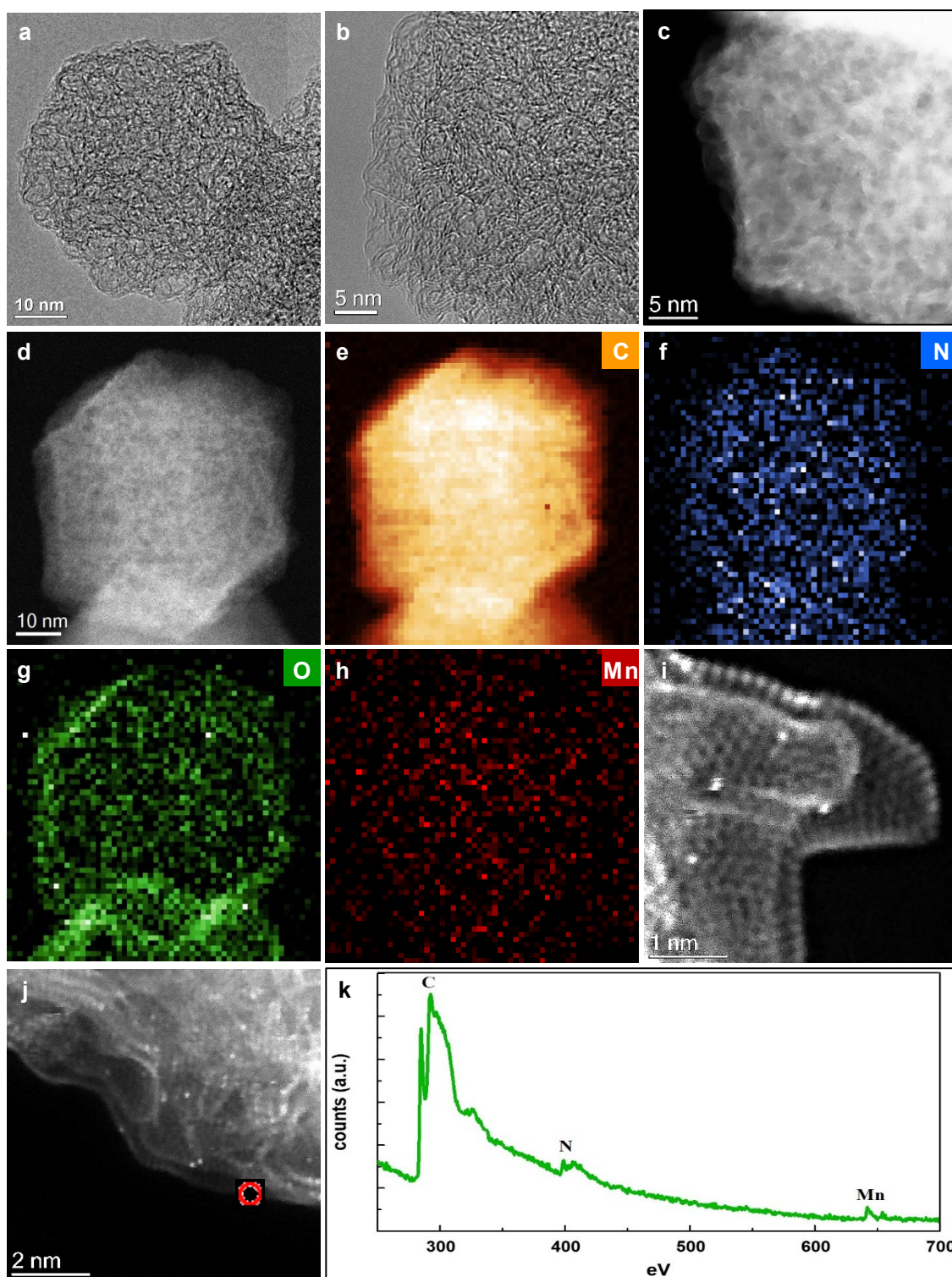
Fig. 3 | Morphology and atomic structure of the 20Mn-NC-second catalyst. Representative HR-TEM (**a, b**) and STEM (**c, d**) images of a carbon particle in the catalyst. **e-h,** EELS elemental maps of C (**e**), N (**f**), O (**g**), and Mn (**h**) of the area in (**d**). **i, j,** aberration-corrected MAADF-STEM images. **k,** EEL point spectrum from the atomic sites circled in red in (**j**). Image resolution in i and j is roughly 0.1 nm using an accelerating voltage of 60 kV.
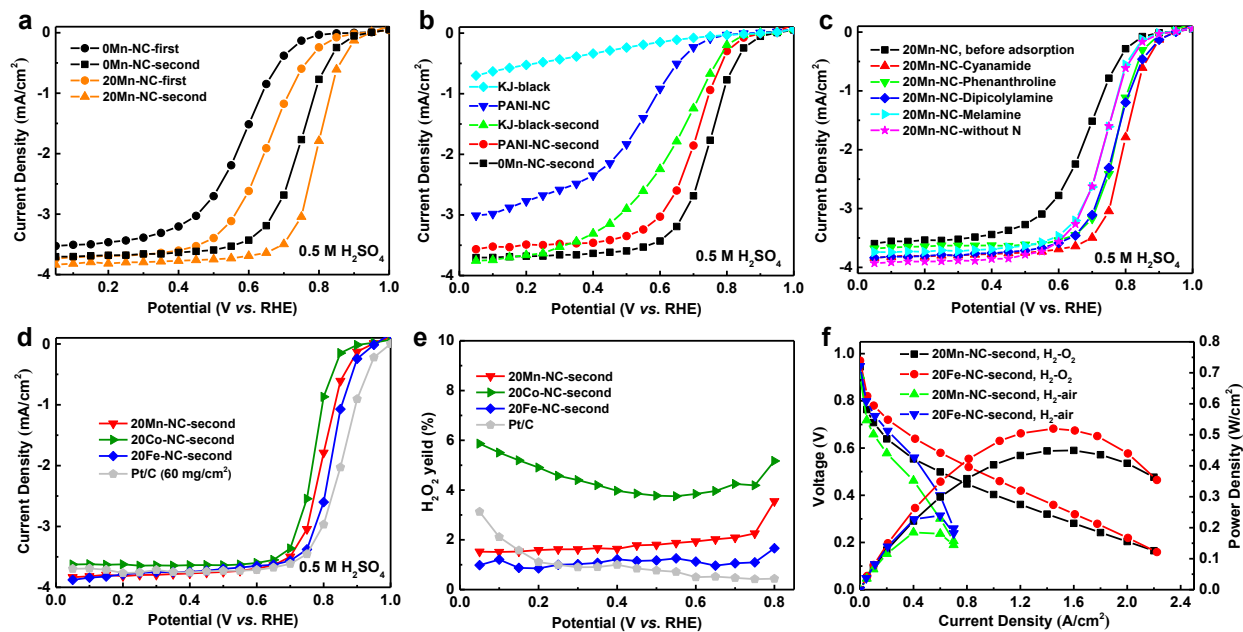
Fig. 4 | ORR activity studied by using RRDE and fuel cell tests. a-d, Steady-state ORR polarization plots in 0.5 M H_2SO_4 electrolytes (Pt/C catalyst reference was studied in 0.1 M $HClO_4$) to study the effect of synthesis steps (*i.e.*, first doping and second adsorption) on Mn-N-C catalyst activity (**a**), effect of various carbon hosts used for the second adsorption step on resultant activity (**b**), effect of different nitrogen sources used for the adsorption step on final catalyst activity (**c**), and comparison of catalytic activity of Fe-, Co-, and Mn-N-C catalysts prepared from identical procedures (**d**). **e,** Four-electron selectivity (*i.e.*, H_2O_2 yields) of the ORR on Fe-, Co-, and Mn-N-C catalysts. **f,** Fuel cell performance of the best performing 20Mn-NC-second and 20Fe-NC-second catalysts in both H_2/O_2 and H_2/air conditions.
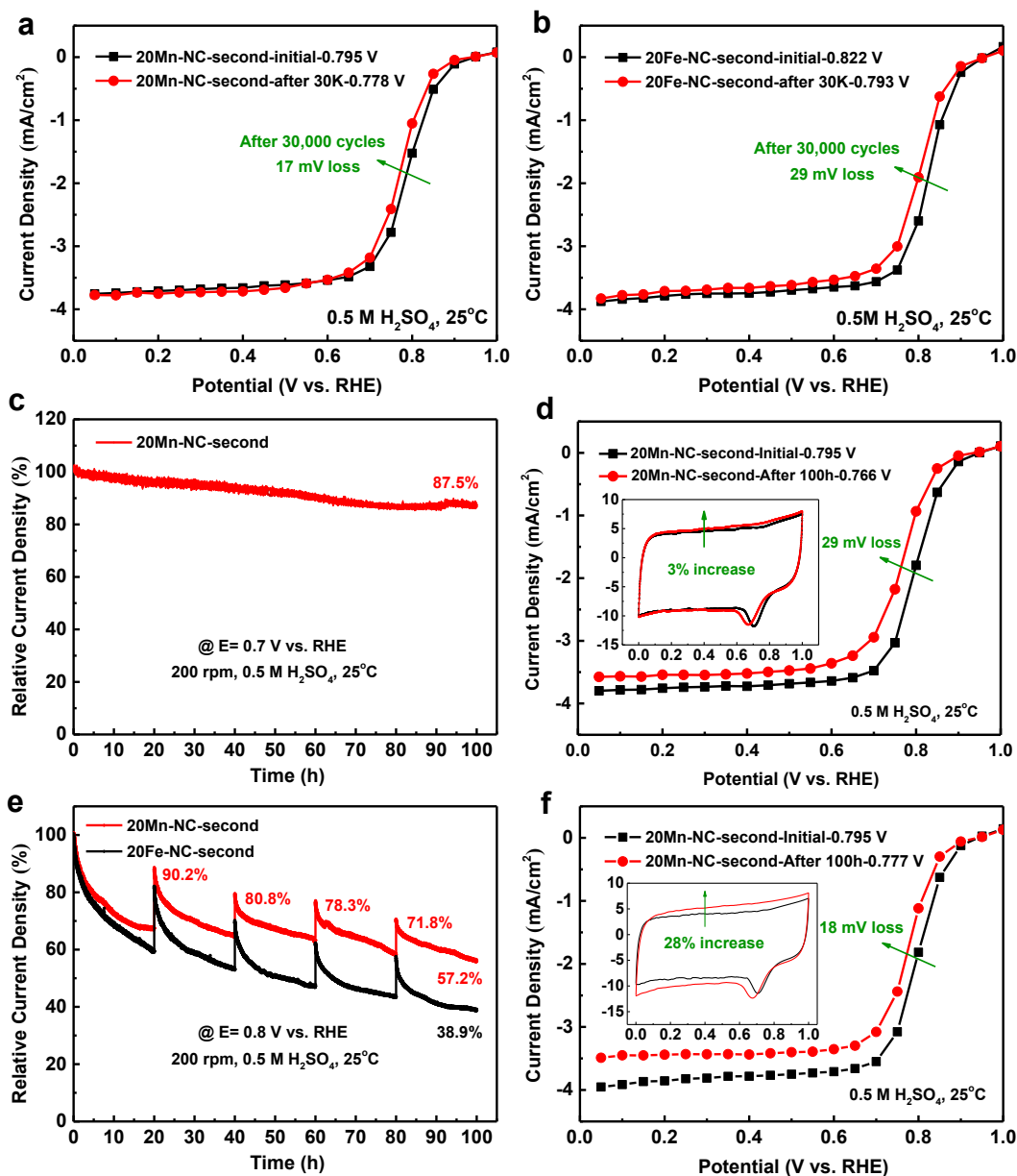
Fig. 5 | Catalyst stability studied by using potential cycling and constant potentials. a-b, Steady-state ORR polarization plots before and after potential cycling stability tests (0.6 V-1.0 V, 30,000 cycles) for the 20Mn-NC-second (**a**) and 20Fe-NC-second catalyst(**b**). **c, e,** i-t curves at constant potentials of 0.7 V (**c**) and 0.8 V (**e**). **d,f,** Steady-state ORR polarization plots and CV curves before and after constant potential tests at 0.7 V (**d**) and 0.8V (**f**) for 100 hours in O_2-saturated 0.5 M H_2SO_4.
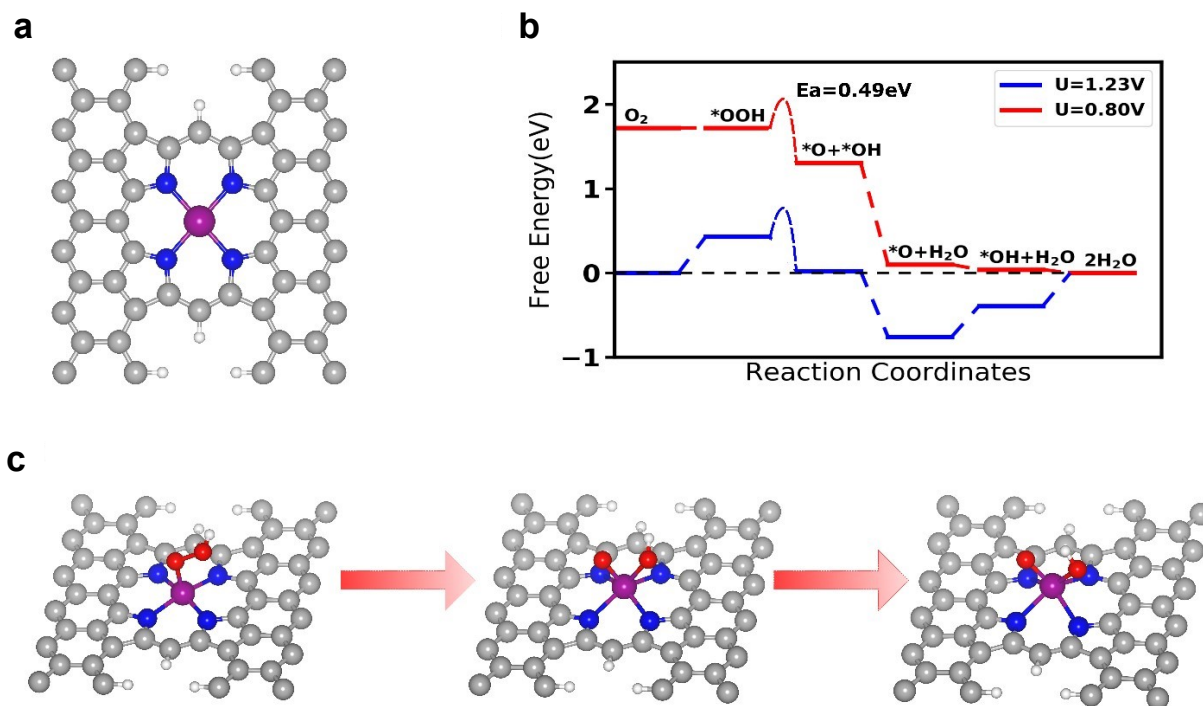
Fig. 6 │ Fundamental understanding on possible Mn active sites by using DFT calculations.

a, Atomistic structure of MnN_4C_{12} active site in the 20Mn-NC-second catalyst. **b,** Calculated free energy evolution diagram for ORR through 4e- associative pathway on the MnN_4C_{12} active site under electrode potential of U=1.23 V and U=0.80 V. **c,** Atomistic structure of initial state (left panel, *i.e.*, state *OOH in **b**), transition state (middle panel), and final state (right panel, *i.e.*, state *O+*OH in **b**) for OOH dissociation reaction on MnN_4C_{12} active site. In this figure, gray, blue, purple, red, and white balls represent C, N, Mn, O, and H atoms, respectively.